J. Fluid Mech. (1994), *vol.* 258, *pp.* 355–370

A determination of the effective viscosity for the Brinkman–Forchheimer flow model

By R. C. GIVLER[1] AND S. A. ALTOBELLI[2]

[1] Engineering Sciences Center, Sandia National Laboratories, Albuquerque, NM 87185, USA

[2] Lovelace Medical Foundation, Albuquerque, NM 87108, USA

The effective viscosity μ_e for the Brinkman–Forchheimer flow (BFF) model has been determined experimentally for steady flow through a wall-bounded porous medium. Nuclear magnetic resonance (NMR) techniques were used to measure non-invasively the ensemble-average velocity profile of water flowing through a tube filled with an open-cell rigid foam of high porosity ($\phi = 0.972$). By comparing these data with the BFF model, for which all remaining parameters were measured independently, it was determined that $\mu_e = (7.5^{+3.4}_{-2.4})\mu_f$, where μ_f was the viscosity of the fluid. The Reynolds number, based upon the square root of the permeability, was 17.

1. Introduction

Steady flow through a wall-bounded porous medium has been modelled by numerous investigators (Larson & Higdon 1986; Durlofsky & Brady 1987; Vafai & Kim 1990; Hsu & Cheng 1990; Kladias & Prasad 1991; Chen & Chen 1992) using some variation of an extended Darcy law. For purposes of this investigation we have chosen the Brinkman–Forchheimer equation, namely

$$0 = -\nabla p + \mu_e \nabla^2 \boldsymbol{v} - \left(\frac{\mu_f \boldsymbol{v}}{k} + \frac{c\rho|\boldsymbol{v}|\boldsymbol{v}}{k^{\frac{1}{2}}}\right), \tag{1}$$

where p is a volume-averaged pressure, $\boldsymbol{v}$ is a volume-average velocity vector, μ_f is the fluid viscosity, ρ is the fluid density, k is the permeability of the porous medium and c is a constant coefficient. Equation (1) describes a balance among the applied fluid pressure gradient and several opposing forces – viscous transfer of momentum and linear and quadratic drag forces. In the event that the applied pressure gradient is exactly offset by the linear drag term, one recovers Darcy's law, which is simply,

$$-\nabla p = \mu_f \boldsymbol{v}/k. \tag{2}$$

The last term in (1) is the Forchheimer drag term to augment Darcy's law when the fluid inertia cannot be neglected. This added correction is generally needed when the Reynolds number of the flow,

$$Re = \rho V k^{\frac{1}{2}}/\mu_f, \tag{3}$$

is greater than unity (Irvine & Hartnett 1978, p. 5). Here, V represents a suitable norm of the vector $\boldsymbol{v}$.

When a porous flow domain contains an interface, such as a wall or adjacent clear fluid region, the second term on the right-hand side of (1) may be important. In this instance, the so-called Brinkman term predicts the development of boundary layers which emanate from the interface. Unfortunately, accurate usage of the

Brinkman–Forchheimer equation has been hampered because of the uncertainty associated with the coefficient μ_e which acts as an effective viscosity. In the case for which the material permeability becomes large, (1) reduces to the Stokes equation and the effective viscosity is the dynamic viscosity of the fluid. Lundgren (1972) has computed values for this coefficient for the cases of flow through a random bed of fixed spheres and of a flowing suspension of spheres. His calculations reveal that in the case of flow through a packed bed, the effective viscosity can be either greater than or less than the fluid viscosity. The result depends upon the volume fraction of spheres, i.e. $(1-\phi)$. It has not been possible to check directly these, and other (Kolodziej 1988; Nield 1991), predictions for μ_e since most experimental work has been performed for geological media which generally possess porosities outside the range for which these theories are valid. Most published work that uses the Brinkman flow model assumes that $\mu_e = \mu_f$.

The purpose of this paper is to describe experimental techniques that were used to determine the effective viscosity coefficient appearing in (1) for wall-bounded flow through a cylindrical plug of porous material. We will describe, in the next section, a non-invasive technique used to measure the ensemble-average velocity profile in the porous material. In the discussion that follows the NMR diagnostic methods, flow experiments are described that were used to measure independently the BFF model parameters: foam porosity ϕ, permeability k and the Forchheimer coefficient c. Then with all parameters of (1) either known or measured independently, save one, it is possible to compute a velocity profile in terms of the sole remaining parameter, μ_e. Model predictions were compared to the measured velocity profile with the choice for the effective viscosity dictated by least-squares error minimization. The proposed value for the effective viscosity is bounded by estimates of the experimental errors. We discuss these and other sources of possible experimental bias. Finally, the results from additional measurements used to obtain the functional dependence of μ_e on flow rate are discussed.

2. Experimental measurements

In this section we describe the various measurement techniques, experimental flow loops and the procedures used to determine the material properties of the porous material. A key ingredient in the determination of the effective viscosity for the BFF model is the ability to measure an averaged velocity profile within a porous medium. We have employed a pulsed-Fourier transform NMR technique (described in §2.1) to measure the velocity profile of water flowing in a cylindrical tube (2.54 cm inside diameter) that has been fitted with a porous plug of 2.54 cm diameter and approximately 15 cm in length. The porous medium used for this study was a reticulated, fully 'open-pore', flexible, ester-type polyurethane foam supplied by the Foamex Company, Eddystone, PA. Nominally, the pore count for this foam was 10 pores per linear inch (p.p.i.) or 4 p.p.cm. This material is also referred to as 'cellular plastic' and is used in household scrubbers, heavy duty air filters and sound suppression applications.

A coarse foam was used because this material possesses a relatively high permeability which, in turn, will produce a rather thick fluid boundary layer adjacent to a solid boundary. Because of the limited resolution of the NMR technique, it was important to have a boundary layer that was between $\frac{1}{16}$ and $\frac{1}{2}$ of the tube radius. Thin boundary layers near the tube wall, associated with low-permeability materials ($k < 1 \times 10^{-5}$ cm^2), would be much harder to resolve with the current NMR method.

The integral foam plug was composed of 16 abutting thin disks. These smaller pieces were die cut from a 9.5 mm thick sheet; it was easier to die cut precisely round disks with perpendicular sidewalls using thin, rather than thick, stock. Before loading into the Plexiglas tube, the foam was coated with a dilute epoxy film by immersing each piece in a solution comprised of the following weight percents: 45% Shell Epon Resin 815, 5% TETA hardener and 50% methylene chloride. Each piece was then blotted and blown with a compressed air jet to clear all pores and minimize the remaining epoxy film thickness. This coating ensured point contact adhesion between the foam skeletal ends and the tube wall. Moreover, the epoxy film, upon curing, imparted added stiffness to the foam. Under nominal flow conditions experienced in this study, we did not observe any deformation of the foam or fluid channelling near the tube wall. We should also note that by constructing a foam plug as described here, there was no variation in the foam porosity near the wall. This is in contrast to packed-sphere systems whose porosity is known to vary markedly as a wall is approached.

2.1. *NMR technique*

Velocity measurements using NMR were performed in the horizontal bore (31 cm diameter) of a superconducting magnet (1.9 Tesla from Oxford Instruments). A 'bird-cage' radiofrequency (rf) probe, tuned to 80.3 MHz (see Watkins & Fukushima 1988), and actively shielded gradient coils (Magnex) were controlled by a versatile VAX-based (Digital Equipment Corp.) image/spectrometer (Quest 4400 from Nalorac Cryogenics Corp.). Data collected by the NMR imager was transferred via Ethernet (Xerox Corp.) to a workstation (Sun Microsystems) for analysis using customized data-reduction software.

NMR imaging experiments make use of the proportionality between NMR frequency ω and the magnetic field B expressed by the Larmor equation $\omega/2\pi = \gamma B$, where γ has the value 42.5 MHz T^{-1} for protons. Gradient coils were used to generate spatially linear variations of the magnetic field $B = (B_0 + G_x x + G_y y + G_z z)$, with concomitant changes in ω. These gradients were small compared to the static field; peak values for the magnetic field gradients used in these experiments were 1–4 mT m^{-1}. NMR signals were induced by the small, transient magnetization resulting from the precession of a large number of nuclear spins. This magnetization was initially excited by an rf pulse, modified by gradient pulses, and then observed in the presence of a 'readout' gradient. The process encoded data from one spatial coordinate in the frequency of the signal and additional spatial (and velocity) information in the phase of the signal. After observation, the magnetization was given time to re-equilibrate. Three crucial aspects of the imaging process may be inferred from these comments. First, information from all locations within the sample was received simultaneously as the NMR signal, which could only be observed when most of the magnetization was nearly in phase. Second, in order to decode the information present in the phase of the signal, repeated measurements with systematic variation of the phase encoding gradients were made. Third, since the velocity and one spatial coordinate were both encoded in the phase of the signal, velocity was extracted from the difference between two signals.

The use of NMR imaging for fluid velocity measurements is relatively new but it is gaining acceptance as the method is improved. Most previous measurements have been taken for simpler flow geometries, i.e. unidirectional flows, where application of the NMR technique is more straightforward (Caprihan & Fukushima 1990). The difficulty in performing NMR measurements for complex flows is an irreversible dephasing of nuclear spins during the time of measurement; this is caused by incoherent motions

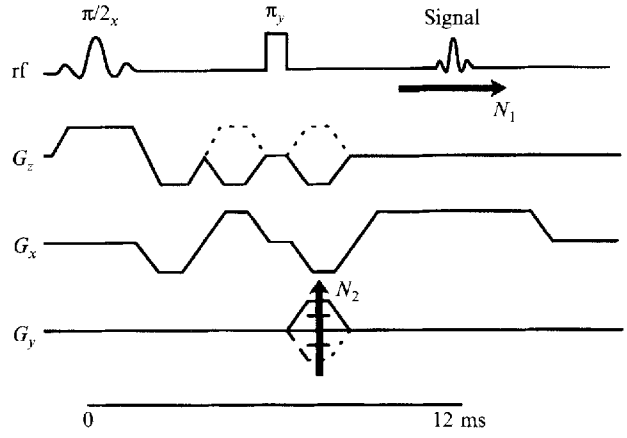

FIGURE 1. Radiofrequency and gradient pulsing sequence for NMR measurement of velocity in the flow experiments.

within an imaging volume (voxel). We have succeeded in making velocity measurements in the porous foam plug for fairly slow flows by using short time intervals between rf pulses. In this work, we used a standard spin-warp rf pulsing sequence combined with the phase method for velocity determination (Caprihan & Fukushima 1990). Spin-echo experiments were needed to reduce the sensitivity of the NMR sequence to overall magnetic field inhomogeneities.

The timing sequence of the rf pulse, the magnetic field gradients, and the resulting NMR signal are shown in figure 1. The amplitude-modulated rf pulse, denoted as $\pi/2_x$, and the first lobe of G_z defined a 5 mm thick NMR slice through a cross-section of the foam plug. Thus, each NMR image comprised a cylindrical volume 2.54 cm in diameter and 0.5 cm in length. The π-pulse produced a spin–echo 12 ms after the centre of the $\pi/2$ pulse. The two G_z pulses flanking the π-pulse control the velocity encoding and were reversed in different experiments as discussed below. G_x encoded one transverse coordinate in the frequency of the signal and G_y imparted a phase shift depending upon the other transverse displacement. For each NMR image produced with this technique, 128 repetitions (N_2) of the basic sequence, differing in the value of G_y, were collected. During each of these repetitions, which were separated by 300 ms, 128 points (N_1) were digitized during the period marked 'signal' in figure 1. The $N_1 \times N_2$ complex array obtained in this manner was converted into an image by a two-dimensional discrete Fourier transform.

Thus, a typical experiment consisted of NMR signals spatially averaged over $0.4 \times 0.4 \times 5$ mm^3 voxels, which were much smaller than the pore size transverse to the flow, but approximately twice the pore size in the flow direction. The NMR measurements also effectively average the signal during the time required to collect the image data. The absence of significant noise in the phase-encode direction of the image is indicative of the steadiness of the flow over this interval (Haacke & Patrick 1986). The timescale on which irreversible dephasing due to convective accelerations occurred was 12 ms, which was short compared to the average transit time through a foam pore.

The voltage profile of the 'readout' gradient G_x was designed to minimize the sensitivity of the NMR signal to the x-component of velocity. A simpler readout waveform suffices for stationary images, but the disordered flow through the tortuous foam plug could not be imaged without a 'balanced' read-profile (Caprihan & Fukushima 1990). Operationally, the stepped gradient G_y can occur at any time during

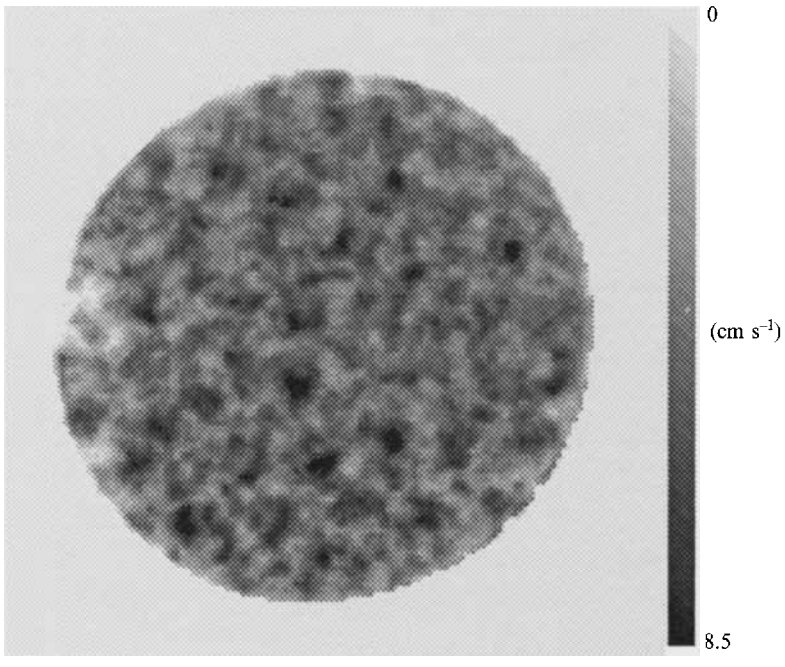

FIGURE 2. NMR grey-scale image of the axial velocity in the porous foam plug. Local velocities range between 0 (white) and 8.5 cm s^{-1} (black) and the average velocity is 6.1 cm s^{-1}.

the NMR sequence. For velocity measurements, however, it is important to place the phase-encoding pulses near the time of echo formation to reduce registration errors which occur when the 'readout' and phase-encode coordinates are recorded at different times.

Ideally the G_z profile shown by the solid line of figure 1 has a zero first moment ($\int tG_z\,dt$) with respect to time, which means that there should be no sensitivity to the z-component of velocity v_z. When the G_z waveform followed the dotted lobes, the NMR experiment should be sensitive to v_z. Because of experimental imperfections, mostly eddy currents induced in the metallic cryostat by the rapidly changing magnetic field gradients, there were small spurious contributions to the image phase which were cancelled with 'extra' reference images. This was accomplished by the following procedure. Four NMR images were recorded for each flow rate and at each selected slice. With no flow, image S_0 was taken with G_z given by the solid line in figure 1, and image S_1 results from the dotted lobes of G_z. Images M_0 and M_1 were obtained using the same G_z profiles while the fluid was moving. Images S_0 and M_0 had inherently low velocity sensitivity compared to S_1 and M_1 which had a velocity sensitivity U of 0.55 cm s^{-1} rad^{-1}.

A new binary image F (essentially a mask) was computed from the moving fluid image M_0 by clipping all values below a minimum threshold intensity. The time-average velocity field was computed from the mask according to

$$\frac{v_z(x,y)}{U} = F \times \mathrm{Arg}\left(\frac{M_1/M_0}{S_1/S_0}\right), \tag{4}$$

where the Arg-function is equivalent to computing the arctangent of the quotient of the imaginary and real images. In these experiments, the fluid velocity and sensitivity were large enough to cause phase wrapping (velocity-induced phase shifts greater than π) in

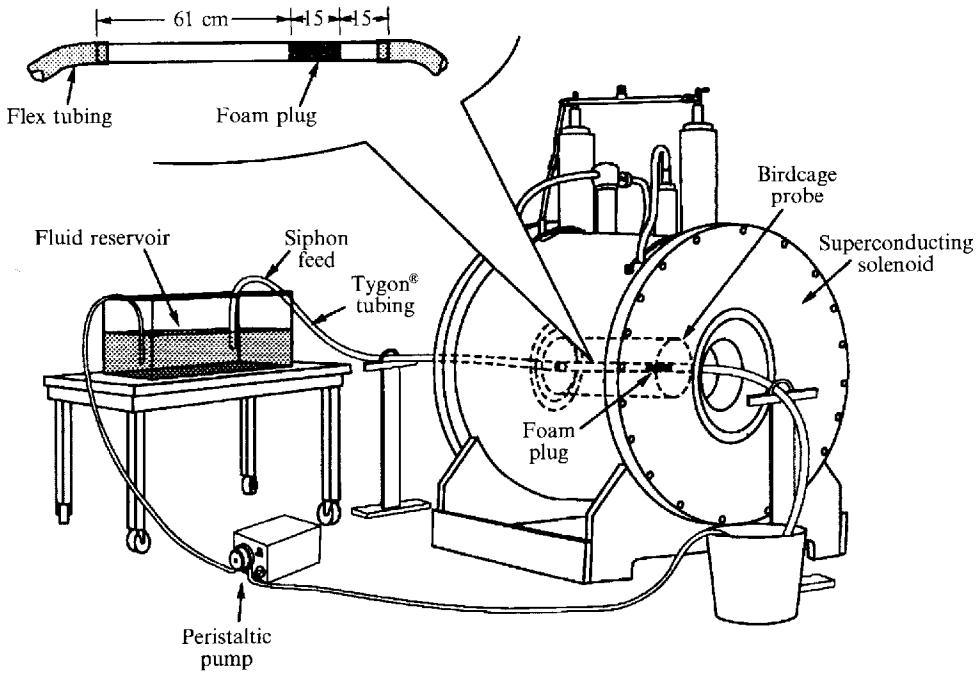

FIGURE 3. Schematic of the flow experiment using NMR to measure the velocity profile within the cylindrical plug of porous foam.

regions of relatively high velocity. Division of the complex data was used rather than subtraction of phases because it reduced the number of phase wraps in the velocity image. These wraps caused discontinuities because the calculated phase jumped between branches of the Arg-function. Points near the tube wall were used to choose the region of the image which received no adjustment and multiples of 2π were added to the phase of the signal in the wrapped regions. A representative unwrapped NMR image of the axial velocity field within the porous foam plug is shown in figure 2.

After the time-average velocity field was calculated and unwrapped, the centroid of the data field was determined from the mask. Data were smoothed by averaging over the angular interval $(0, 2\pi)$. The number of data points used to calculate each azimuthal average was proportional to the distance from the centroid and ranged from four values at the centreline to approximately 200 at the tube wall. The results of this averaging process are the radial profiles of axial velocity displayed in figures 4 and 5.

2.2. *Measured velocity profiles*

Figure 3 illustrates the laminar, open-flow loop that was used to make velocity measurements with the NMR technique. Water was siphoned from a constant-head reservoir, flowed in a tube that passed through the bore of a superconducting solenoid, and drained into a collection bucket. It was returned to the reservoir by a peristaltic pump. The water was slightly doped with gadopentate dimeglumine to improve its NMR signal characteristics. The accepted values for the density and viscosity of water were not affected by the added dopant. The flow path was composed of flexible transparent tubing except for a 60 cm length of rigid tubing that was the test section in the centre of the magnet. The flexible tubing was affixed to a backing board both upstream and downstream from the test section to ensure straight and parallel flow in the test section. The flow rate was adjusted with a throttling valve and was measured

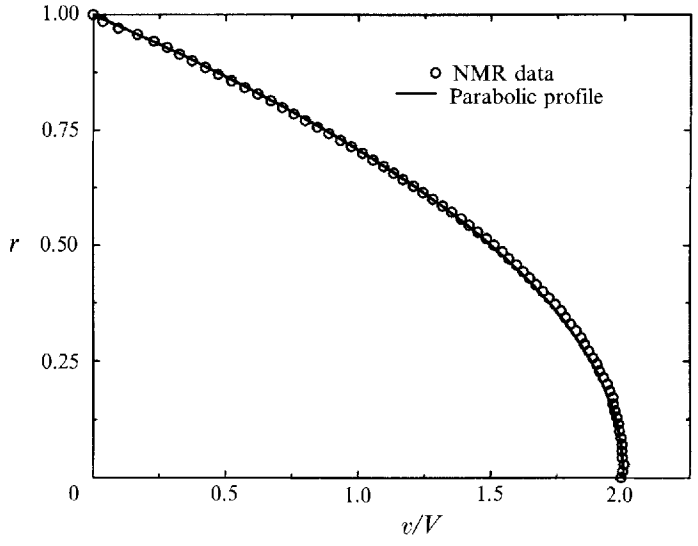

FIGURE 4. Hagen–Poiseuille velocity profile measured with NMR.

by timed collection of a given volume of liquid. NMR data collection time for an average experiment was about 4 minutes.

The measured velocity profile for steady flow in the unobstructed portion of the tube, 18 cm upstream from the fitted foam plug, is plotted in figure 4. We anticipate that the fluid velocity at this location should be unaffected by the porous obstruction and is accurately described by the Hagen–Poiseuille velocity profile. The three-dimensional NMR velocity information recorded during this experiment has been averaged both in the azimuthal and axial (through the tagged slice thickness) coordinates and then plotted as a one-dimensional velocity profile in figure 4. Agreement between the NMR data and the expected paraboic profile is excellent. The resolution of the NMR technique for these flow experiments can be inferred from the data presented in the figure; about 70 data points span the tube radius. The average velocity V as measured by time collection was 2.91 cm s^{-1}.

Figure 5 illustrates an ensemble-average velocity profile within the porous plug for an identical flow rate. In addition to the azimuthal and axial averaging of the NMR data over the selected slice dimensions, the profile plotted in figure 5 is the superposition of data from six different axial locations within the porous plug. The selected axial locations were separated by 2 cm, thereby effectively sampling the entire usable porous test section. Velocity measurements were not taken near the entry or exit flow regions in the foam. This overall ensemble-averaging procedure yields a smoothly varying velocity profile as seen in figure 5. Some noise in the data is still evident near the centre of the tube. This is a manifestation of the azimuthal averaging process combined with the inhomogeneity of the foam; data near the centreline are not smoothed nearly as much as velocity information near the tube wall. Hence, several large pores near the tube centre can still impart aberrations to the averaged profile. Averaging among more axial locations would further improve the flatness of this profile near the tube centre. A predicted velocity profile from the BFF model, representing a 'best-fit' approximation, is plotted for comparison with the NMR data in figure 5. Details regarding its computation are explained in §3.

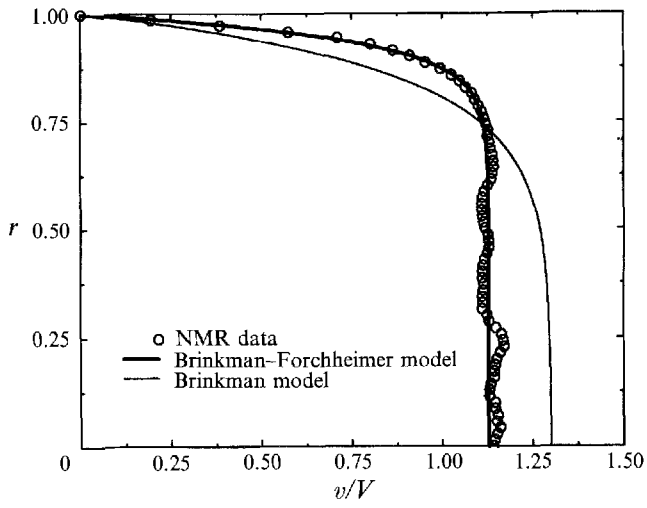

FIGURE 5. Velocity profiles in wall-bounded flow through a cylindrical foam plug.

2.3. *Measurement of model parameters*

The techniques and procedures used to measure foam properties are discussed briefly in the following paragraphs. The particular choice of material, namely 10 p.p.i. reticulated foam, made some of these measurements difficult. We have already mentioned that the choice of coarse foam facilitated the velocity profile measurements; however, the flow resistance offered by this material made measuring its permeability difficult. In fact, several methods were tried before arriving at a scheme that yielded accurate measurements. Initially, it was thought that the permeability of the foam could be obtained by blowing air through a thick sample and simultaneously measuring the pressure gradient and flow rate. At low flow rates, exceedingly small pressure differences were difficult to measure accurately. At high flow rates, considerable deformation of the foam sample was observed. This technique was not pursued.

Later, we tried to measure k from foam settling experiments; a thin sheet of foam ($30 \times 30 \times 2.5$) cm^3 was allowed to settle through a water/glycerine bath. If one ignores edge effects (i.e. assumes one-dimensional flow through the foam), then the terminal velocity of the falling sheet can be related to its permeability. Although many runs were tried, it was difficult to get the foam to settle uniformly without tilting. Alternatively, we tried to pull the sheet of foam upward through the liquid bath with a supporting undercarriage. In any event, detailed numerical simulations indicated that flow through the foam near its edges was not unidirectional and, hence, this technique provided only crude estimates for the permeability.

2.3.1. *Porosity*

The porosity of the polyurethane foam was measured with a pseudo-pycnometry technique using isopropyl alcohol ($CH_3CHOHCH_3$) intrusion. One problem that plagues accurate porosity measurements is the entrapment of small air bubbles during immersion. Alcohol proved to be a far superior wetting liquid than did water, displacing all observable air bubbles.

Linear dimensions and mass of a large rectangular block of foam were recorded from which one can compute a bulk foam density ρ_b. The bulk density of the foam was found to be $0.0333^{+0.0006}_{-0.0006}$ g cm^{-3} (see §4 for an explanation of this notation). Next a

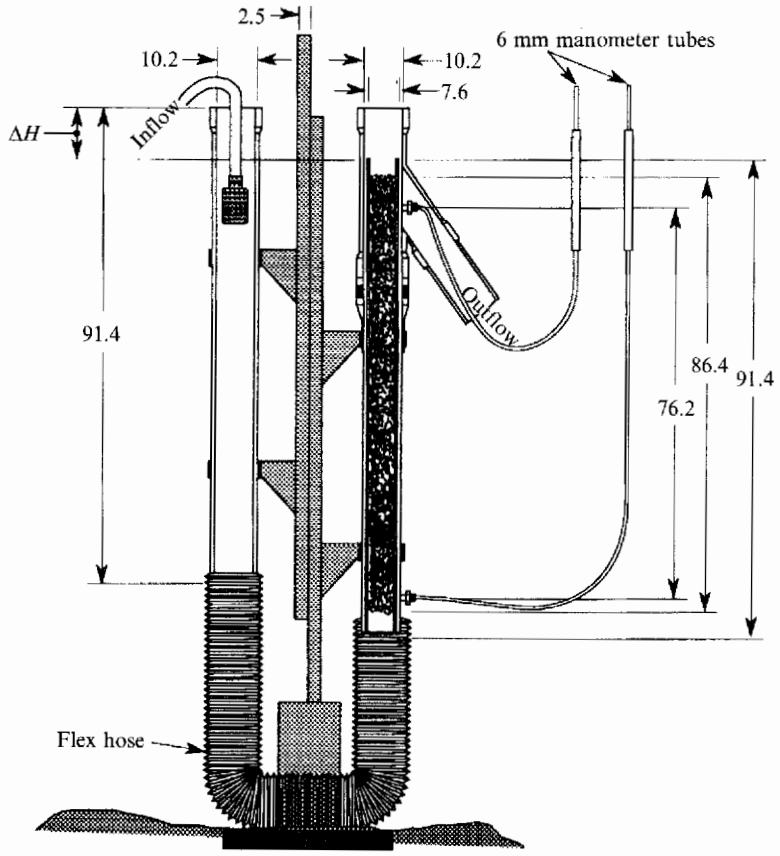

FIGURE 6. Flow apparatus used to measure the permeability of open-cell foam. Dimensions in cm.

known mass of foam (5–10 g) was immersed in 500.0 cm^3 of isopropyl alcohol thereby displacing a measurable mass of liquid. The volume occupied by the foam skeletal network was then computed from the mass of the displaced alcohol and its measured material density. Four separate trial runs were performed to determine the porosity, which yielded $\phi = 0.972^{+0.0003}_{-0.0020}$. From these data it follows that the specific density of the skeletal material was $\gamma_s = 1.19^{+0.01}_{-0.04}$.

2.3.2. *Permeability*

Permeability of the foam was determined independently by using pressure loss versus flow rate measurements which were performed with the apparatus shown in figure 6. The open-flow loop designed for this purpose was a large-diameter, U-tube configuration – two vertically-oriented rigid pipes, mounted side by side and open at their tops, were connected at their lower ends via a flexible hose. The pressure gradient for water flowing upward through the column of foam was measured directly with an inclined differential manometer. The flow rate was measured by timed collection of the efflux and was altered by adjusting the relative heights of the inlet (serving as a reservoir) and outlet pipes. Excess water delivered to the inlet spilled over the pipe rim, thus maintaining a constant head.

The foam column was composed of seventeen circular disks fitted inside a clear plastic pipe. These disks were cut from a 5.08 cm thick foam sheet; rough-cut pieces were trimmed to precise circular disks by using a special purpose jig that rotated the

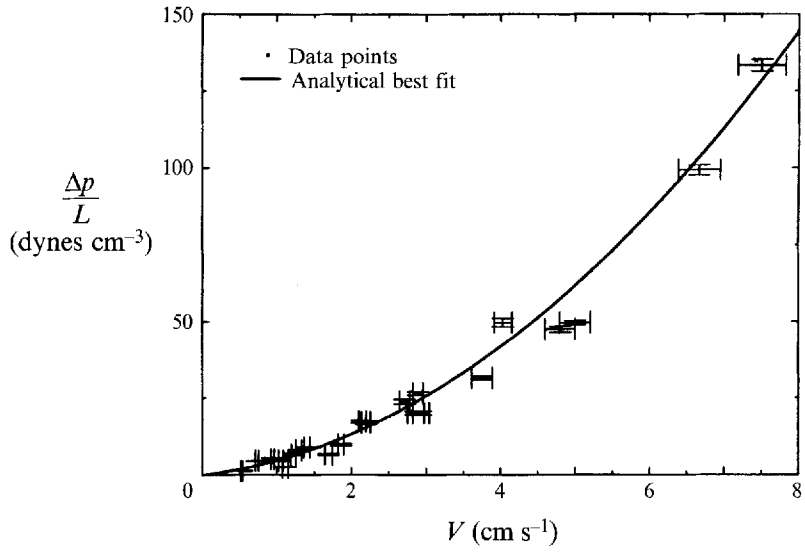

FIGURE 7. Pressure loss *vs.* average velocity for water flowing through 10 p.p.i. open-cell foam.

foam past a knife-edged band saw blade in a circular pattern. The final diameter of the foam disks was 2 mm greater than the inside diameter of the confining pipe. This ensured a snug fit against the pipe walls without having to glue the individual foam pieces in place. Again, no distortion of the foam was observed during these flow experiments.

Pressure loss plotted against the average velocity in the foam is shown in figure 7. This figure is a superposition of raw data from two separate trial runs. Here, the average velocity was obtained by dividing the flow rate by the cross-sectional area. In so doing, we neglected the boundary-layer effects that are known to be present at the walls. However, this effect was made small by choosing a pipe with a fairly large diameter, in this case 7.46 cm. By neglecting the wall boundary layer, the average velocities were underestimated by, at most, 4%. This error was estimated *a posteriori* by computing the boundary-layer displacement thickness, $\delta = 0.074$ cm. Thus, given a pipe diameter of 7.46 cm, the difference between the geometric cross-sectional area (43.7 cm^2) and the effective cross-sectional area (42.0 cm^2) is 3.9%. Error bars in both the x and y measured values are depicted in figure 7. They result from a propagation of systematic experimental errors; other sources of error will be discussed in §4.

Since the wall effects are small in the foam column for the flow apparatus of figure 6, we assume that the data can be described by a one-dimensional Forchheimer-extended, Darcy law given by

$$\frac{-\Delta p}{L} = \frac{\mu_f V}{k} + \frac{c\rho V^2}{k^{\frac{1}{2}}}, \tag{5}$$

where Δp is the pressure differential recorded by the dual-mounted manometers and L is the distance between tap locations. Using the experimental data illustrated in figure 7, it is possible to determine numerical values for k and c. To accomplish this, we rewrite (5) as

$$\frac{-\Delta p}{LV} = \frac{c\rho}{k^{\frac{1}{2}}} V + \frac{\mu_f}{k}, \tag{6}$$

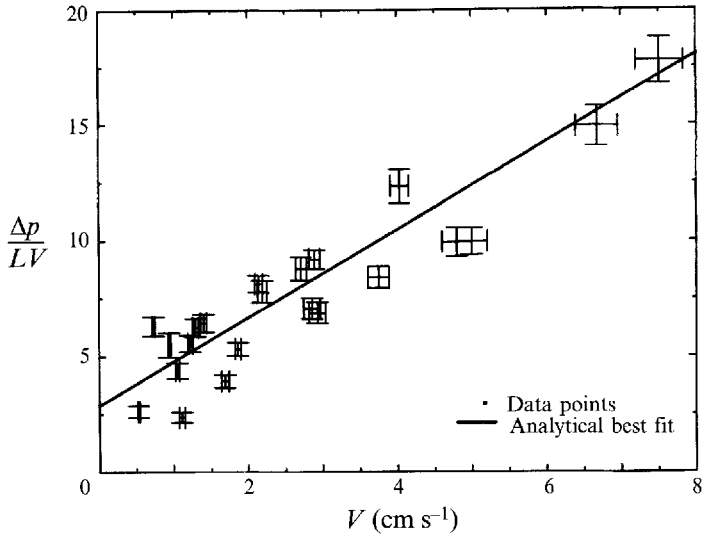

FIGURE 8. Flow measurements which determine the permeability of 10 p.p.i. open-cell foam.

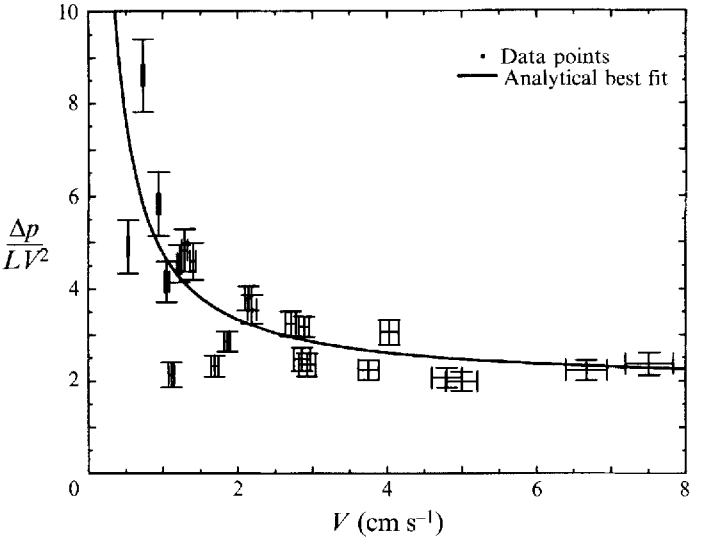

FIGURE 9. Flow measurements which determine the Forchheimer coefficient for 10 p.p.i. open-cell foam.

which is an equation for a straight line in the variables V and $-\Delta p/LV$. Experimental data plotted in this manner are illustrated in figure 8. A straight line indicating the least-squares best fit is also illustrated. It follows from (6) that the intercept between this curve and the ordinate axis is the quantity μ_f/k which was determined to be $2.86^{+0.55}_{-0.55}$. The error estimate represents one standard deviation between the analytical best fit and the experimental data. It is evident from the error bar estimates of figure 8 that the uncertainty due to the scatter in the data (produced by two separate trial runs) dominates the uncertainties produced by propagation of systematic errors. Hence, the error estimates in the quantity μ_f/k reflect this fact. The viscosity of water was taken to be $0.93^{+0.04}_{-0.04}$ cP for these flow experiments and so the permeability for the foam was calculated to be $0.0033^{+0.0009}_{-0.0006}$ cm^2.

2.3.3. *Coefficient of the Forchheimer term*

The experimental data may be further manipulated by dividing (6) by the average velocity to yield a new dependent variable, namely

$$\frac{-\Delta p}{LV^2} = \frac{\mu_f}{kV} + \frac{c\rho}{k^{\frac{1}{2}}}, \tag{7}$$

the results of which are plotted in figure 9. From (7) it is seen that for large V the data tend to be an asymptote of $c\rho/k^{\frac{1}{2}}$; the value for this quotient was estimated graphically to be $1.9^{+0.4}_{-0.4}$. The density of water was taken to be $0.9975^{+0.0004}_{-0.0004}$ g/cm^3 which, when taken with the experimentally determined value for the permeability, yields a value for the Forchheimer coefficient of $0.11^{+0.04}_{-0.03}$. In each of figures 7–9, the analytical best fit curve was drawn from (5) with $\mu_f/k = 2.86$ and $c\rho/k^{\frac{1}{2}} = 1.9$.

3. Numerical model predictions

The main objective of this paper is the evaluation of the BFF model for water flowing through a cylindrical porous plug. A direct evaluation of the effective viscosity can be made if one compares the measured velocity profile obtained with the NMR technique with the velocity distribution predicted by (1). A 'best fit' value for μ_e can be chosen by minimizing the residual error between (1) and the NMR experimental data for the velocity profile.

In cylindrical coordinates, the radial variation of the ensemble-average velocity on the interval $r = (0, 1)$ is given by

$$\frac{\mathrm{d}^2 v}{\mathrm{d}r^2} + \frac{1}{r}\frac{\mathrm{d}v}{\mathrm{d}r} - a_1 v - a_2 v^2 = a_0, \tag{8}$$

where

$$a_0 = \frac{R^2}{\mu_e}\frac{\Delta p}{\Delta z}, \tag{9}$$

$$a_1 = \frac{\mu_f}{\mu_e}\frac{R^2}{k}, \tag{10}$$

and

$$a_2 = \frac{c\rho R^2}{\mu_e k^{\frac{1}{2}}}, \tag{11}$$

where R is the tube radius. Equation (8) is subject to the following boundary conditions:

$$v(1) = 0 \quad \text{and} \quad \frac{\mathrm{d}v}{\mathrm{d}r}(0) = 0. \tag{12}$$

An analytic solution to the linear flow model derived from (8) for the limiting case of low flow rate does exist. Here, the inertial correction afforded by the Forchheimer term is not taken into account. In this instance the fluid velocity profile in a tube is given by

$$v = -\frac{\Delta p}{\Delta z}\frac{k}{\mu_e}\left[1 - \frac{I_0(a_1^{\frac{1}{2}} r)}{I_0(a_1^{\frac{1}{2}})}\right], \tag{13}$$

where I_0 is a modified Bessel function. For comparative purposes the normalized velocity profile given by (13), using $a_1 = 65$, is plotted in figure 5 and denoted as the

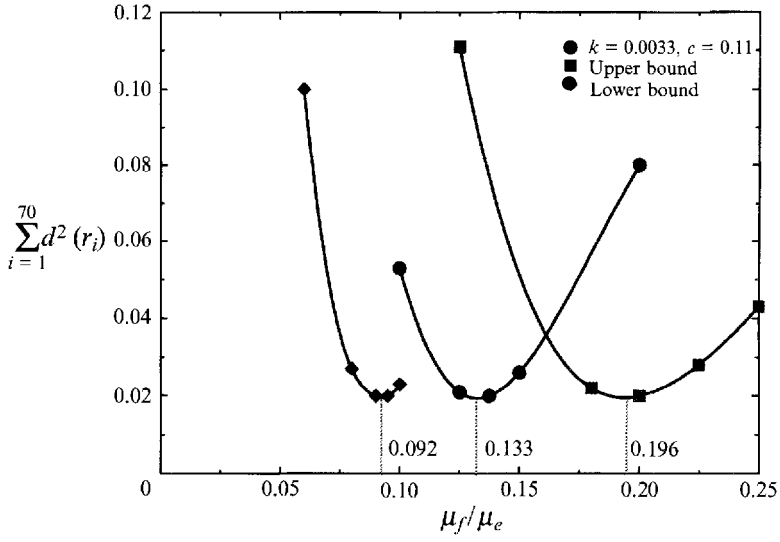

FIGURE 10. Least-squares error minimization to determine the 'best fit' value for the viscosity ratio.

Brinkman flow model. From this comparison of velocity profiles the mathematical role of the Forchheimer term is made clear; fluid inertia flattens the normalized velocity profile by decreasing the boundary layer.

The nonlinear problem, (8) with (12), was integrated numerically with a shooting method to obtain the velocity profile within the foam plug for conditions identical to those in the NMR experiments. The pressure gradient $\Delta p/\Delta z$ was adjusted to achieve a flow rate of 14.7 $cm^3\ s^{-1}$. This corresponds to a value of $Re = 17$ which matches the experimental conditions. Several choices for the value of the effective viscosity were searched in an effort to minimizc E, the sum of squared differences d between model predictions and experimental data. In this manner, the value for the effective viscosity was determined by least-squares error minimization. Results from a parameter estimation analysis are illustrated in figure 10, which indicate that the optimal choice for the viscosity ratio is $\mu_f/\mu_e = 0.133$. Error bounds for the viscosity ratio are computed based upon the uncertainties in the measured quantities k and c. These bounding curves are also plotted in figure 10. The effective viscosity for the BFF model is thus calculated to be $(7.5^{+3.4}_{-2.4})\mu_f$.

Additional experimental measurements of the effective viscosity were recorded for both lower and higher flow rates. We followed the same data-reduction procedure as previously outlined to determine the effective viscosity of the BFF model for each respective flow rate; the results are illustrated in figure 11. The measurement errors associated with each data point in figure 11 make it difficult to draw a conclusion regarding the precise flow rate dependency of the effective viscosity. It does appear qualitatively that the effective viscosity is rather insensitive to the flow rate for $Re < 20$ and increases with increasing flow rate when $Re > 20$. Since the effective viscosity does not appear to be a material constant for all Reynolds numbers, as one would like in the case of the BFF model, the data of figure 11 point to a deficiency in the BFF model, at least for strongly inertial flows. Conversely, figure 11 indicates the flow regime, $Re < 20$, where the BFF model is validated by an effective viscosity that does not vary with flow rate. Measurements of the effective viscosity for additional flow rates and for other porous materials are needed to support the limited findings presented here.

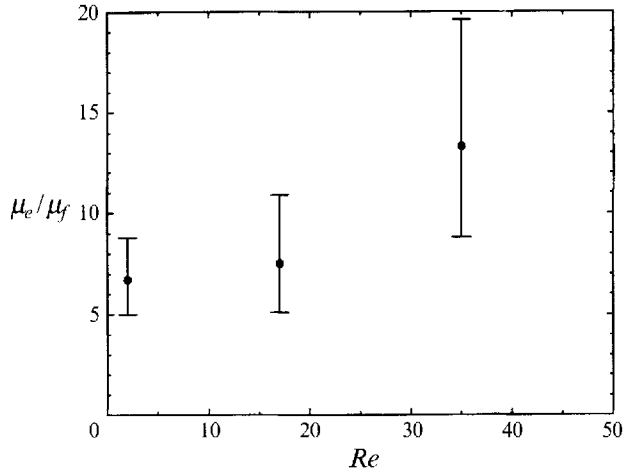

FIGURE 11. Flow rate dependency of the effective viscosity for the BFF model.

4. Error estimates

We have been careful to affix error estimates to all measured quantities or parameters that have been derived from measured data. Errors bars have been used for plotted data while numerical values have been reported in the format, $x = x_{0-B}^{+A}$, which should be interpreted as $(x_0 - B) \leqslant x \leqslant (x_0 + A)$. The error estimates A and B result from a propagation of systematic errors (examples of which are the uncertainty associated with reading a rule to make a length measurement or the timing inaccuracies in using a stopwatch), and have been calculated by standard techniques (Shoemaker, Garland & Steinfeld 1974, p. 51).

In addition to the systematic errors that are present in these experiments, some sources of random errors should also be noted. The experimental data plotted in figure 7 provide a good illustration of random errors. From this plot it is clear that all data points do not lie on the analytical 'best fit' curve – even taking the error bars into account. As mentioned in the reporting of those permeability measurements, this collection of data was the result of two separate trial runs. In each case the foam column was disassembled and repacked after which the flow loop was primed. The scatter in the data of figure 7 reflects the random errors as a result of repeating the experiment. The modest scatter in these data may have been caused by the trapped air bubbles in the foam column. Attempts were made to remove the air bubbles during priming by pre-washing the foam with soapy water. While this exercise helped, it was noted that some small air bubbles were always visible during the experiments.

We have not performed an error analysis for the velocity data taken with the NMR scheme. We believe that any errors, both systematic and random, in these data are small in comparison with those associated with the parameters in the BFF model. Thus, the error tolerances quoted for the effective viscosity of the BFF model are dominated by the uncertainties associated with measuring the foam properties. Substantial confidence is imparted to the NMR velocity measurement scheme by comparing data for fully developed pipe flow with the analytical Poiseuille velocity profile as illustrated in figure 4. The agreement between data and predictions is excellent.

We also mention that some small random errors may be attributable to foam inhomogeneities and local property variations within the foam itself. These could be

due to incomplete opening of all the foam cells or anisotropy imparted to the foam from the manufacturing process. Also, the nature of the manufacturing process makes it difficult to replicate exactly identical foam properties from batch to batch. In fact, the foam used for the NMR velocity measurements and that used for material property determination were obtained from separate batches. Both samples, however, were rated at 10 p.p.i. according to manufacturer's specifications and were visually identical.

5. Conclusions

NMR techniques have been used to measure non-invasively the fluid velocity profile for water flowing in a wall-bounded porous medium. It does appear from the results plotted in figure 5 that the BFF model describes the flow through this wall-bounded foam plug exceedingly well. Using these data, the effective viscosity μ_e for the Brinkman–Forchheimer flow model has been calculated to be 7.5 times that for the fluid viscosity μ_f for $Re = 17$. Error estimates indicate that this value is bounded by the limits ($5.1 \leqslant \mu_e/\mu_f \leqslant 10.9$). The effective viscosity appears to be insensitive to flow rate for $Re < 20$ but increases modestly for increasing flow rates beyond $Re > 20$. For wall-bounded flows through 10 p.p.i. open-cell reticulated foam it is not appropriate to assume $\mu_e = \mu_f$ for the Brinkman–Forchheimer flow model.

This study determined the effective viscosity for the BFF model from measured values for the permeability, Forchheimer coefficient and the *in-situ* velocity profile. The present NMR technique had a spatial resolution such that the boundary layer was defined by about 15 data points (cf. figure 5). Thus, additional resolution would be needed for parametric studies which vary the porosity and permeability of the foam, at least for the cases of thinning boundary layers. With the present technology, improvement in resolution by a factor of 5 or 6 is available with a time penalty of four fold – not an unreasonable trade-off for additional experiments.

The authors wish to thank Frank Chavez, SNL, who assisted with the porosity and permeability measurements. Also, Charles Hickox, David McTigue and David Gartling, all from SNL, Eiichi Fukushima, Arvind Caprihan and Lee Wang, all from LMF, and Jasper Jackson added much to this work with many helpful discussions and reviews of the manuscript. The polyurethane foam was supplied by Clem Herbst, Foamex Company. This work was supported, in part, by the US Department of Energy (DOE) by Grant No. DE-AC04-76DP00789 and its Office of Basic Energy Sciences via Grant No. DE-FG04-90ER14087. Financial support does not constitute an endorsement by DOE of the views and opinions expressed in this article by the authors.

REFERENCES

CAPRIHAN, A. & FUKUSHIMA, E. 1990 Flow measurements by NMR. *Phys. Rep.* **198**, 195–235.

CHEN, F. & CHEN, C. F. 1992 Convection in superposed fluid and porous layers. *J. Fluid Mech.* **234**, 97–119.

DURLOFSKY, L. & BRADY, J. F. 1987 Analysis of the Brinkman equation as a model for flow in porous media. *Phys. Fluids* **30**, 3329–3341.

HAACKE, E. M. & PATRICK, J. L. 1986 Reducing motion artifacts in two-dimensional Fourier transform imaging. *Magn. Reson. Imaging* **4**, 359–376.

HSU, C. T. & CHENG, P. 1990 Thermal dispersion in a porous medium. *Intl J. Heat Mass Transfer* **33**, 1587–1597.

IRVINE, T. F. & HARTNETT, J. P. 1978 *Advances in Heat Transfer*, Vol. 4, Academic.

KLADIAS, N. & PRASAD, V. 1991 Experimental verification of Darcy–Brinkman–Forchheimer flow model for natural convection in porous media. *J. Thermophys.* **5**, 560–576.

KOLODZIEJ, J. A. 1988 Influence of the porosity of a porous medium on the effective viscosity in Brinkman's filtration equation. *Acta Mechanica* **75**, 241–254.

LARSON, R. E. & HIGDON, J. J. L. 1986 Microscopic flow near the surface of two-dimensional porous media. Part I. Axial flow. *J. Fluid Mech.* **166**, 449–472.

LUNDGREN, T. S. 1972 Slow flow through stationary random beds and suspensions of spheres. *J. Fluid Mech.* **51**, 273–299.

NIELD, D. A. 1991 The limitations of the Brinkman–Forchheimer equation in modeling flow in a saturated porous medium and at an interface. *Intl J. Heat Fluid Flow* **12**, 269–272.

SHOEMAKER, D. P., GARLAND, C. W. & STEINFELD, J. I. 1974 *Experiments in Physical Chemistry*, 3rd edn. McGraw-Hill.

VAFAI, K. & KIM, S. J. 1990 Fluid mechanics of the interface region between a porous medium and a fluid layer – an exact solution. *Intl J. Heat Fluid Flow* **11**, 254–256.

WATKINS, J. C. & FUKUSHIMA, E. 1988 High-pass, birdcage coil for nuclear magnetic resonance. *Rev. Sci. Instrum.* **59**, 926–929.